Journal of Engineering Mathematics (2005) 52: 99–126
DOI 10.1007/s10665-004-3686-9

Starting flow generated by the impulsive start of a floating wedge

A. IAFRATI and A.A. KOROBKIN[1]
INSEAN Italian Ship Model Basin, Via di Vallerano, 139 - 00128, Rome, Italy (a.iafrati@insean.it); [1]Lavrentyev Institute of Hydrodynamics, Novosibirsk 630090, Russia (kaa@hydro.nsc.ru)

Received 30 June 2003; accepted in revised form 16 July 2004

Abstract. The initial stage of the plane unsteady flow caused by the impulsive vertical motion of a wedge initially floating on an otherwise flat free surface is investigated with the help of a combination of numerical and asymptotic methods. The liquid is assumed ideal and incompressible and its flow potential. Compressible effects give a negligible contribution to the flow close to the entering body at the stage considered in the present paper. The vertical velocity of the body is constant after the impulsive start. The flow domain is divided into an outer region, where the first-order solution is given by the pressure-impulse theory, and inner regions close to the intersection points between the free surface and the moving body. The relative displacement of the body plays the role of a small parameter. The inner solution is matched with the outer one. The outer solution is given in quadratures but the inner solution, which is shown to be nonlinear and self-similar, can be found only numerically. With the aim of deriving the inner solution, the inner region is divided into three parts. In the far-field zone the solution is given in terms of its asymptotic behavior while, in the jet region, attached to the wedge, the flow is described by a second-order shallow-water approximation. In the intermediate region a boundary-element method is used, which is suitably coupled with the solutions in both the jet and the far-field regions through an iterative pseudo-time stepping procedure. The procedure is dependent on the deadrise angle of the wedge. If the angle is equal or smaller than $\pi/4$, eigensolutions appear in the far-field asymptotics and their amplitudes are recovered together with the solution. The approach is applied to different values of the wedge deadrise angle. The obtained results can be used to improve the prediction of the hydrodynamic loads acting on floating bodies, the velocity of which changes rapidly.

Key words: boundary-element approaches, free-surface flows, matched asymptotic expansions, water impact

1. Introduction

The unsteady flow caused by an impulsive vertical motion of a floating flared body is considered. The motivation for this research comes from naval hydrodynamics, where ships may undergo sudden motions in the vertical plane, giving rise to high hydrodynamic loads. Such loads occur mainly at the bow part of the ship, which is usually flared. The wedge is considered here as the simplest representation of flared bodies and the impulsive vertical motion of a floating wedge represents a sudden change of the velocity of a ship section.

The present paper is focused on the understanding of the initial transient stage after the impulsive start of a wedge floating on a liquid surface, when the initial draft of the body matters. The study is carried out within the framework of potential flow of ideal and incompressible fluid without both surface-tension and gravity effects and the entry velocity is assumed to be constant.

The unsteady flow caused by a sudden motion of a floating body is usually described by using the pressure-impulse concept. This approach provides the flow pattern near the body after a short compressible stage [1]. However, in the case of a flared body, the pressure-impulse solution is not uniformly valid close to intersection points between the free surface of the liquid and the body surface where the liquid velocity exhibits a singularity.

The difficulties with the initial asymptotics appear even in the case of non-flared bodies. For example, the plane problem of a semi-submerged circular-cylinder impact was numerically solved by Vinje and Brevig [2] and by Faltinsen [3]. The computed hydrodynamic forces are rather different. Vinje [4] wrote "The difference between the two solutions seems to appear in the second derivative of the force at time equal to zero.... the different ways Faltinsen and Vinje & Brevig treated the intersection point problem might very well explain the difference between the results. A solution of the "inner" problem might resolve this question, but so far this solution has not been calculated; what has been published so far is based on linear theory." This observation shows the importance of the initial asymptotics of the flow and, in particular, of the "inner" solutions near the intersection points for numerical simulations of the impact.

The leading-order "inner" solution of the flow near the intersection points in the case of a semi-submerged circular-cylinder impact has been derived recently in [5]. This inner solution was matched to the second-order outer solution. It should be noted that the singularity appears in the second-order outer solution of the problem but the first-order outer solution is regular [4]. In order to answer the question raised in [4] about the initial asymptotics of the hydrodynamic force on a vertically moving cylinder, higher-order inner and outer solutions are required, at least up to the fourth-order of the outer solution. The fourth-order uniform asymptotics of the solution has not been derived so far.

As an example of a flow where the first-order outer solution is already singular, a small-time expansion procedure has been used in [6] to study the flow induced by a vertical plate uniformly accelerating from the rest in a stationary fluid under the action of gravity. A uniformly valid solution has been derived by using the method of the matched asymptotic expansions.

In the case of a flared-body impact the first-order outer solution is singular. The first-order outer solution of the problem of floating-wedge impact was obtained by Sedov [7]. One may expect that the corresponding "inner" solution, describing the flow near the intersection points, much stronger affects the total hydrodynamic force on the entering body than in the case of semi-submerged-cylinder impact. We are unaware of any results on the flow near the intersection point of a flared body starting to move suddenly. These results could be helpful, not only for study of starting flows but also for numerical simulations of the developed flows.

In order to obtain a uniformly valid description of the flow during the initial stage, an inner solution is considered near the intersection points within stretched variables (Section 4). Taking the ratio between the vertical displacement of the wedge and its initial draft as a small parameter, it is shown that the inner solution is approximately self-similar, nonlinear and depends only on the deadrise angle of the wedge. For the determination of the inner solution the corresponding boundary-value problem is reformulated with the help of a modified velocity potential which drastically simplifies the boundary conditions on the free surface, whose shape is unknown in advance and has to be determined as part of the solution.

To compute the first-order inner solution, a numerical pseudo-time stepping procedure is developed. The procedure is based on the boundary-integral representation of the velocity potential. The asymptotic behavior of the solution in the far field is recovered in Section 5 and is used to provide improved boundary conditions at the far field boundary of the reduced computational domain and a first guess of the free-surface shape. A shallow-water model is presented in Section 6 aimed at simplifying the solution of the flow in the thin jet layer. An improved version of this model, which is presented in the appendix, is directly incorporated into the numerical solver, thus yielding a significant reduction in the computational effort needed to describe the flow field in the thin jet region. The numerical model is presented in Section 7 and results are shown in Section 8, along with their careful verification.

In the case of constant entry velocity, it is believed that the fluid flow in a later stage of the evolution is quite independent of the flow details at the initial phase. This means that, when the vertical displacement of the wedge becomes much larger than its initial draft, the solution is expected to approach the classical self-similar solution of the wedge-entry problem [8]. The first-order small-time approximation employed here does not allow a verification of this point. Large-time asymptotics of the floating-wedge-impact solution is required, which can be obtained only by numerical analysis of the developed flow.

Although the case of the floating wedge is considered here as a representative of flared bodies, generalization of the results obtained below to both more complicated shapes and three-dimensional configurations is straightforward and is discussed briefly in the concluding section.

2. Formulation of the problem

The starting flow caused by unsteady interaction between the liquid and a floating wedge is considered (see Figure 1). Initially, both the liquid and the body are at rest. Let $x_c = h_0 \cot \gamma$, where γ is the deadrise angle and h_0 is the initial draft of the wedge. The part of the liquid boundary $|x| > x_c$, $y = 0$ corresponds to the free surface, where the pressure is zero at all times. The points $(-x_c, 0)$ and $(x_c, 0)$ are referred to as the left- and right-hand side intersection points, respectively. At some instant of time, taken as initial ($t = 0$), the wedge suddenly begins to move down with a constant velocity V. The wedge is rigid and the flow is plane, irrotational and symmetric with respect to the axis $x = 0$. The liquid is assumed ideal and incompressible. External mass forces and surface-tension are neglected at the initial stage under consideration in the present study. We shall determine the liquid flow and the shape of the liquid free surface during the initial stage, when $Vt/h_0 \ll 1$, with special attention given to the fine pattern of the flow near the intersection points.

In this paper the deadrise angle γ is positive and less than $\pi/2$. The limiting cases $\gamma \ll 1$ and $\pi/2 - \gamma \ll 1$ are not considered. The case of a floating-wedge impact with a small deadrise angle, $\gamma \ll 1$, was studied by Oliver [9] within the Wagner approach [10]. The case $\gamma \to \pi/2$ corresponds to the vertical-plate impact, the initial asymptotics for which was given in [6].

The liquid flow is described by the velocity potential $\phi(x, y, t)$, for which the initial-boundary-value problem has the form

$$\phi_{xx} + \phi_{yy} = 0 \qquad (\text{in} \quad \Omega(t)), \tag{1}$$

$$\phi_y = \phi_x \tan\gamma - V \quad (\text{on} \quad \Gamma_b(t)), \tag{2}$$

$$2\phi_t + \phi_x^2 + \phi_y^2 = 0 \quad (\text{on} \quad \Gamma_f(t)), \tag{3}$$

$$H_t + \nabla H \cdot \nabla \phi = 0 \quad (\text{on} \quad \Gamma_f(t)), \tag{4}$$

$$H(x, y, -0) = 0, \quad \phi(x, y, -0) = 0, \tag{5}$$

$$\phi(x, y, t) \to 0 \quad (x^2 + y^2 \to \infty), \tag{6}$$

where $\Omega(t)$ is the fluid domain at instant t. The boundary of the flow region consists of two parts: the free surface $\Gamma_f(t)$ described by the equation $H(x, y, t) = 0$, where the function $H(x, y, t)$ has to be determined together with the velocity potential, and the entering body surface $\Gamma_b(t)$ given by the equation $y = |x| \tan\gamma - h_0 - Vt$. On the wetted part of the body surface $\Gamma_b(t)$ condition (2) has to be satisfied, which implies that the normal component of

the velocity of the body and that of the liquid particles are equal to each other. On the free surface $\Gamma_f(t)$ dynamic (3) and kinematic (4) boundary conditions hold. Condition (6) implies that far from the moving body the liquid is at rest at any time. The initial conditions (5) state that the liquid is at rest before impact. Once problem (1–6) has been solved, the velocity field $\mathbf{u}=(u, v)$, $u=\phi_x$, $v=\phi_y$, and the hydrodynamic pressure $p(x, y, t)=-\rho_0(\phi_t+\frac{1}{2}|\nabla\phi|^2)$, where ρ_0 is the liquid density and $\nabla\phi=(\phi_x, \phi_y)$, can be evaluated.

In the following, the initial asymptotics of the liquid flow is derived with the aim of clarifying the flow pattern close to the intersection point during an early stage of the motion when the displacement of the wedge is still rather smaller than its initial submergence, that is $Vt/h_0 \ll 1$. This is achieved by using the pressure-impulse theory which can be considered as the first-order approximation within the small-time expansion procedure. According to this procedure, the solution of the boundary-value problem (1–6) is sought in the form

$$\begin{aligned} &\phi(x, y, t)=[\phi_0(x, y)+\phi_1(x, y)t+\phi_2(x, y)t^2+\cdots]\chi(t),\\ &H(x, y, t)=y-f(x, t),\\ &f(x, t)=[f_1(x)t+f_2(x)t^2+\cdots]\chi(t), \end{aligned} \tag{7}$$

where $\chi(t)=1$ when $t>0$ and $\chi(t)=0$ when $t\le 0$. Substituting Equation (7) in equations (1–4) and (6), expanding the boundary conditions (2) and (3) about the initial position of the boundary of the liquid region (this technique is known as the Stokes procedure) and collecting terms of the same order as $t\to 0$, we arrive at boundary-value problems for unknown harmonic functions $\phi_j(x, y)$ in the region $\Omega(0)$ and the functions $f_j(x)$, where $x>x_c$ and $j\ge 0$.

The small-time expansion procedure was effectively used by Ovsyannikov [11] in the nonlinear problem of a bubble raising toward the liquid free surface and by Tyvand and Miloh [12] in the problem of a circular submerged cylinder starting to move impulsively. In all these problems there are no intersection points between the body and the free surface. The method is very powerful. In particular, Ovsyannikov [11] proved that the solution obtained with the help of the small-time expansion procedure is an analytical function of time and the blow-up instant for the obtained solution was estimated. It is expected that similar results can be obtained also for the problem of circular-cylinder motion beneath the free surface, where the third-order solution as $t\to 0$ was derived in [12].

In the problem of flared-body impact the small-time expansion procedure cannot be used in its classical form as represented by expansions (7). This is due to the fact that a solution of the form (7) is singular at the intersection points and has to be considered an "outer" solution. Near the intersection points an "inner" solution has to be introduced. Considering time t as a small parameter in (1–6), we can conclude that the problem is singularly perturbed. According to the theoretical background of asymptotic methods (see, [13] and [14]), one needs, first, to construct the first-order outer solution $\phi_0(x, y)$, which is the solution given by the pressure-impulse theory; second, to find the first-order inner solution in a small vicinity of the intersection points and to match it with the first-order outer solution. Then one needs to determine the second-order outer solution and match it with the first-order inner solution. We cannot guarantee in advance that the second-order outer expansion of the velocity potential will be of the order of $O(t)$ as it is shown in expansion (7). This is because there is a possibility that the effect of the inner solution on the outer solution is so strong that already the second-order term of the velocity potential in the outer region is determined by details of the flow near the intersection points. Then one needs to obtain the second-order inner solution and match it with the second-order outer solution, and so on. Proceeding thus, one can derive accurate and uniformly valid initial asymptotics of the flow caused by floating-body

impact. Using this asymptotics is suggested instead of the initial conditions (5) to start reliable numerical simulations of the impact problem and to improve predictions of the hydrodynamic loads on floating flared bodies.

The technique described above is known as the method of matched asymptotic expansions. The procedure of matching was suggested by Poincare (see, [13]). For the floating-wedge-impact problem the first-order outer solution was given by Sedov [7] and it can also be found in a recent paper by Mei, Liu and Yue [15]. The corresponding inner solution can only be determined numerically. This solution is valid at the intermediate stage when $V/c_0 \ll tV/h_0 \ll 1$. In this paper we restrict ourselves to the first-order inner solution of the original problem (1–6) while focussing on the main features of both the flow and the free-surface shape close to the intersection points.

From a rigorous mathematical point of view the construction of the uniformly valid asymptotic solution is a first necessary step, upon which the obtained asymptotic solution has to be justified. In order to justify the asymptotic solution, one has to (i) prove that the solution of the original problem (1–6) exists, is unique and is continuously dependent on the parameters of the problem; (ii) formulate the boundary-value problem with respect to the auxiliary functions which represent the difference between the exact and the asymptotic solution; (iii) obtain uniformly valid estimates for these auxiliary functions; (iv) demonstrate that the auxiliary functions tend to zero faster than both the exact and the asymptotic solution. It is seen that a complete rigorous analysis of the initial impact stage is divided into two parts: (1) construction of the uniformly valid asymptotic solution, which is usually performed with the help of methods of asymptotic analysis (see, [13]) and (2) justification of the obtained asymptotic solution using the theory of boundary-value problems. The present paper deals only with the first step of this program.

3. First-order outer solution

In accordance with the general theory of asymptotic methods, by substituting (7) in Equations (1–6) and letting t tend to zero, we find to leading order

$$\begin{aligned}
&\frac{\partial^2\phi_0}{\partial x^2}+\frac{\partial^2\phi_0}{\partial y^2}=0 \quad (\text{in } \Omega(0)),\\
&\frac{\partial\phi_0}{\partial y}=\frac{\partial\phi_0}{\partial x}\tan\gamma - V \quad (y=|x|\tan\gamma - h_0,\ |x|<x_c),\\
&\phi_0=0, \quad f_1(x)=\frac{\partial\phi_0}{\partial y} \quad (y=0,\ |x|>x_c),\\
&\phi_0\to 0 \quad (x^2+y^2\to\infty).
\end{aligned} \tag{8}$$

The solution of the boundary-value problem (8) was obtained by Sedov [7] in the form

$$\phi_0+\mathrm{i}\psi_0=\mathrm{i}V(z-\frac{l}{w}\sqrt{\tau^2-1}), \tag{9}$$

where $\psi_0(x, y)$ is the stream function, $z=x+\mathrm{i}y$, $l=h_0/\sin\gamma$ is the distance from the wedge apex to the intersection point $(x_c, 0)$, $\tau=\tau(z)$ is the complex function defined by the equation

$$z=-\mathrm{i}h_0+\frac{l}{w}\mathrm{e}^{\mathrm{i}\gamma}\int_0^{\tau}\left(\frac{\tau_0^2}{1-\tau_0^2}\right)^{\frac{\gamma}{\pi}}\mathrm{d}\tau_0 \tag{10}$$

and $w(\gamma)$ is given as

$$w(\gamma)=\int_0^1\left(\frac{\tau_0^2}{1-\tau_0^2}\right)^{\frac{\gamma}{\pi}}\mathrm{d}\tau_0=\frac{1}{\sqrt{\pi}}\Gamma\left(\frac{1}{2}+\frac{\gamma}{\pi}\right)\Gamma\left(1-\frac{\gamma}{\pi}\right). \tag{11}$$

Sedov's solution (9) predicts an unbounded velocity of the flow close to the intersection points $x=\pm x_c$, $y=0$. Due to the flow symmetry, only the right-hand-side intersection point, $x=x_c$, $y=0$, is considered below. Equation (10) shows that $\tau(x_c)=1$ at that point, and $\tau=1+\epsilon$, where ϵ is a new complex variable, $|\epsilon|\ll 1$, in a small vicinity of the right-hand-side intersection point. Substituting $\tau=1+\epsilon$ and $\tau_0=1+\epsilon\delta$ in (10) and using (11) and the equality

$$\int_0^{\tau}\left(\frac{\tau_0^2}{1-\tau_0^2}\right)^{\frac{\gamma}{\pi}}\mathrm{d}\tau_0=w+\epsilon\mathrm{e}^{-\mathrm{i}\gamma}\int_0^1\frac{(1+\epsilon\delta)^{\frac{2\gamma}{\pi}}\mathrm{d}\delta}{(2+\epsilon\delta)^{\frac{\gamma}{\pi}}(\epsilon\delta)^{\frac{\gamma}{\pi}}},$$

we find to leading order as $|\epsilon|\to 0$

$$z-x_c=\frac{h_0}{w\sin\gamma}\frac{\pi\epsilon^{\frac{\beta}{\pi}}}{2^{\frac{\gamma}{\pi}}\beta}[1+o(1)], \tag{12}$$

where $\beta=\pi-\gamma$. Solution (9) can be presented in the form

$$\phi_0+\mathrm{i}\psi_0=\mathrm{i}Vx_c+\mathrm{i}V[z-x_c-l\epsilon^{\frac{1}{2}}(2+\epsilon)^{\frac{1}{2}}/w],$$

where $z-x_c=O(\epsilon^{\frac{\beta}{\pi}})=o(\epsilon^{\frac{1}{2}})$ as $|\epsilon|\to 0$ due to the inequality $\beta>\frac{\pi}{2}$. Therefore,

$$\phi_0+\mathrm{i}\psi_0\sim\mathrm{i}Vx_c-\mathrm{i}V\frac{l}{w}(2\epsilon)^{\frac{1}{2}} \tag{13}$$

for small ϵ. Equations (12) and (13) give to leading order as $|\epsilon|\to 0$:

$$\phi_0+\mathrm{i}\psi_0\sim-\mathrm{i}Vh_0^{1-\sigma_0}F(\gamma)(z-x_c)^{\sigma_0}+\mathrm{i}Vx_c,$$

where $\sigma_0=\pi/(2\beta)$ and $F(\gamma)=\sigma_0^{-\sigma_0}(w\sin\gamma)^{\sigma_0-1}$. Taking the real part of the latter asymptotic formula, we finally arrive at

$$\phi_0\sim-Ar^{\sigma_0}\cos(\sigma_0\theta), \tag{14}$$

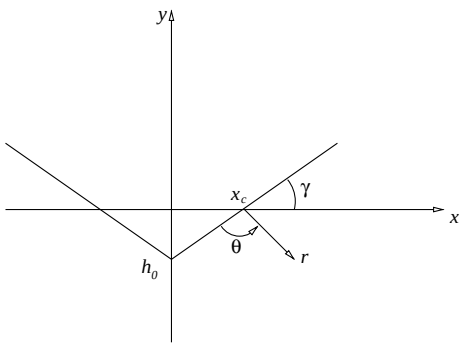

Figure 1. Sketch of the floating wedge in the physical frame of reference.

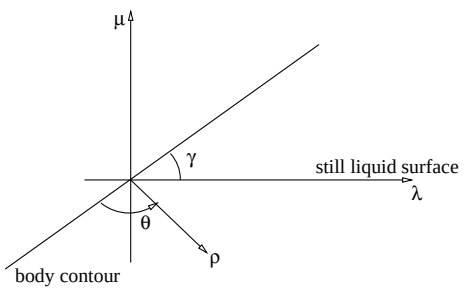

Figure 2. Sketch of the floating wedge in the stretched variable plane.

where $A = VF(\gamma)h_0^{1-\sigma_0}$ and r, θ are polar coordinates such that $z - x_c = re^{i\theta}e^{-i\beta}$, with the origin at the intersection point, $\theta = 0$ on the wedge surface and $\theta = \beta$ on the still liquid surface. The asymptotic behavior of the free surface elevation as $Vt/h_0 \to 0$ and $r/h_0 \to 0$ is described by the equality

$$y = A\sigma_0 r^{\sigma_0 - 1} t[1 + o(1)], \tag{15}$$

which follows from the kinematic boundary condition (4) and the asymptotics of the velocity potential (14). Since $0 < \gamma < \pi/2$, we find

$$\frac{\pi}{2} < \beta < \pi, \quad \frac{1}{2} < \sigma_0 < 1. \tag{16}$$

Inequalities (16) and the asymptotic formulae (14) and (15) imply that Sedov's solution predicts a non-physical flow field with unbounded velocities of the liquid particles on the free surface close to the intersection point. In order to resolve the flow singularity in a small vicinity of the intersection point and provide uniformly valid asymptotics of the solution, which can be used for further numerical calculations, an inner solution has to be introduced.

4. First-order inner solution

The inner solution is sought within the stretched local coordinates λ, μ which are introduced as follows (see Figure 2)

$$x = x_c + a(t)\lambda, \quad y = a(t)\mu, \quad \rho = \sqrt{\lambda^2 + \mu^2}, \tag{17}$$

where $a(t) \to 0$ as $t \to 0$, in the form

$$\phi(x, y, t) = Aa^{\nu}(t)\varphi(\lambda, \mu, t), \tag{18}$$

$$H(x, y, t) = \eta(\lambda, \mu, t). \tag{19}$$

The constant ν and the function $a(t)$ have to be determined from the matching condition. The function $\varphi(\lambda, \mu, t)$ is referred to as the inner velocity potential and the unknown function $\eta(\lambda, \mu, t)$ describes the free-surface shape in the local coordinates.

The matching condition implies that the local asymptotics of the first-order outer velocity potential (14), rewritten in the local stretched coordinates (17), matches representation (18) as $\rho \to \infty$ but $a(t)\rho \to 0$. Comparing (14) and (18), we conclude that the matching condition is satisfied if $\nu = \sigma_0$ and

$$\varphi \sim -\rho^{\sigma_0} \cos(\sigma_0 \theta) \quad (\rho \to \infty) \tag{20}$$

for the inner velocity potential.

Substituting Equations (17) and (18) in the dynamic boundary condition (3), we obtain

$$\sigma_0 \varphi + \frac{1}{2} A \frac{a^{\sigma_0}}{a\dot{a}} |\nabla \varphi|^2 = \lambda \varphi_\lambda + \mu \varphi_\mu - \frac{a}{\dot{a}} \varphi_t, \tag{21}$$

where dot stands for the time derivatives. In Equation (21) the quantity

$$\frac{a/\dot{a}}{Aa^{\sigma_0}/(a\dot{a})} = \frac{1}{A} a^{2-\sigma_0}$$

tends to zero as $a(t) \to 0$. Therefore, the term in Equation (21) with the time derivative can be neglected in the leading order comparing to the nonlinear term as $t \to 0$. The nonlinear term is of the same order as other terms in Equation (21) if

$$\frac{\mathrm{d}\, a}{\mathrm{d}\, t} = A a^{\sigma_0 - 1}.$$

If the nonlinear term is small compared to the linear ones as $t \to 0$, we arrive at the linear inner problem, which cannot help us to resolve the flow singularity near the intersection point. If the linear terms in (21) are of higher orders compared to the nonlinear term, then there is no hope to satisfy condition (20) and match the inner solution to the outer one. The differential equation for the function $a(t)$ with account for the initial condition $a(0) = 0$ provides

$$a(t) = [(2 - \sigma_0) A t]^{\frac{1}{2-\sigma_0}}. \tag{22}$$

We conclude that the dynamic boundary condition on the free surface can be approximated during the initial stage as

$$\sigma_0 \varphi + \frac{1}{2} |\nabla \varphi|^2 \approx \lambda \varphi_\lambda + \mu \varphi_\mu \tag{23}$$

in a small vicinity of the intersection point. The dimension of this vicinity is of the order of $O[a(t)]$, where the function $a(t)$ is given by formula (22).

Correspondingly, the kinematic boundary condition (4) can be rewritten as

$$\nabla \eta \cdot \nabla \varphi = \lambda \eta_\lambda + \mu \eta_\mu - \frac{a}{\dot{a}} \eta_t$$

within the local coordinate system, where Equations (19) and (22) were taken into account. The ratio $a/\dot{a}$ is equal to $(2 - \sigma_0)t$ and in the leading order as $t \to 0$ the term with the time derivative can be neglected, thus leading to

$$\nabla \eta \cdot \nabla \varphi \approx \lambda \eta_\lambda + \mu \eta_\mu. \tag{24}$$

The Laplace equation (1) keeps its form

$$\varphi_{\lambda\lambda} + \varphi_{\mu\mu} = 0 \tag{25}$$

in the stretched coordinates, and the boundary condition (2) gives

$$\varphi_\mu = \varphi_\lambda \tan\gamma - \frac{V}{A} a^{1-\sigma_0} \quad (\mu = \lambda \tan\gamma - V t / a(t)),$$

which, in the leading order as $t \to 0$, provides

$$\varphi_\mu = \varphi_\lambda \tan\gamma \quad (\mu = \lambda \tan\gamma). \tag{26}$$

The performed analysis indicates that the first-order inner solution does not depend on time but only on the spatial stretched variables λ and μ. This implies that the starting flow close to the intersection point is self-similar and nonlinear in the leading order as $t \to 0$.

The liquid flow in a small vicinity of the intersection point is approximately described within the local polar coordinates ρ, θ by the velocity potential $\varphi(\rho, \theta)$, the boundary-value

problem for which has the form

$$\Delta\varphi = 0 \quad (\text{in } \Omega_i), \qquad \frac{\partial\varphi}{\partial\theta} = 0 \quad (\mu = \lambda\tan\gamma),$$

$$\sigma_0\varphi + \frac{1}{2}|\nabla\varphi|^2 = \rho\frac{\partial\varphi}{\partial\rho} \quad (\text{on } \Gamma_i), \tag{27}$$

$$\nabla\eta\cdot\nabla\varphi = \rho\frac{\partial\eta}{\partial\rho} \quad (\text{on } \Gamma_i), \qquad \varphi \sim -\rho^{\sigma_0}\cos(\sigma_0\theta) \quad (\rho\to\infty),$$

where the flow domain Ω_i is bounded by the rigid wall, $\mu = \lambda\tan\gamma$, on the left and by the free surface Γ_i on the top. It should be noted that the variables in the "inner" problem (27) are non-dimensional. The position of the free surface close to the intersection points is described by the equation $\eta(\rho,\theta) = 0$.

The boundary-value problem (27) is not easy to solve because the position of the free surface Γ_i is unknown in advance and must be determined as a part of the solution. Without introducing any further approximation, it is useful to rewrite the boundary-value problem (27) in terms of a modified velocity potential $S(\lambda,\mu)$ such that

$$S(\lambda,\mu) = \varphi(\lambda,\mu) - \frac{1}{2}\rho^2. \tag{28}$$

This new unknown function satisfies the Poisson equation

$$\Delta S = -2 \quad (\text{in } \Omega_i). \tag{29}$$

Moreover, Equation (28) provides $\nabla\eta\cdot\nabla\varphi = \nabla\eta\cdot\nabla S + \rho(\partial\eta/\partial\rho)$, which makes it possible to present the kinematic boundary condition as $\nabla\eta\cdot\nabla S = 0$. Therefore, the normal derivative of the function $S(\lambda,\mu)$ vanishes on the liquid free surface

$$S_n = 0 \quad (\text{on } \Gamma_i). \tag{30}$$

The dynamic boundary condition becomes

$$\sigma_0\left(\frac{\rho^2}{2} + S\right) + \frac{1}{2}\left((\lambda + S_\lambda)^2 + (\mu + S_\mu)^2\right) = \rho\left(\rho + S_\rho\right),$$

which gives

$$\frac{\sigma_0}{2}\rho^2 + \sigma_0 S + \frac{1}{2}\left[\rho^2 + 2\rho S_\rho + |\nabla S|^2\right] = \rho^2 + \rho S_\rho.$$

Since $|\nabla S|^2 = S_n^2 + S_\tau^2$ on the free surface, where S_τ is the derivative along the boundary and $S_n = 0$ due to (30), the previous equation takes the form

$$S_\tau^2 + 2\sigma_0 S = (1-\sigma_0)\rho^2 \quad (\text{on } \Gamma_i). \tag{31}$$

In terms of the new velocity potential the body boundary condition reads

$$S_n = 0 \quad (\mu = \lambda\tan\gamma). \tag{32}$$

Finally, the condition at infinity (20) yields

$$S \sim -\frac{1}{2}\rho^2 - \rho^{\sigma_0}\cos(\sigma_0\theta). \tag{33}$$

Two boundary-value problems have been introduced to describe the same solution. The first, (27), deals with the Laplace equation but the boundary conditions are rather complicated. The second deals with the Poisson equation (29), the boundary conditions for which are much simpler. It is important to notice that, once the free-surface shape is known, the function $S(\lambda, \mu)$ along the free surface can be obtained by integration of the boundary condition (31) with account taken of (33). Then the velocity potential $\varphi(\lambda, \mu)$ and its normal derivative φ_n on the free surface can be recovered with the help of Equations (28) and (30). The velocity field in the inner region can be evaluated numerically thereafter using Green's theorems.

It is important to notice that the boundary-value problem (27) looks like that describing the self-similar flow caused by wedge entry at a constant velocity. However, there are several specific features of the boundary-value problem (27), which force us to study this problem independently on the well developed theory of wedge-entry: (1) the dynamic boundary condition in (27) is identical to that for the wedge-entry problem if and only if $\sigma_0 = 1$; in this case Equation (31) can be integrated analytically, which essentially simplifies the following analysis; (2) the body boundary condition in the wedge-entry problem is non-homogeneous; the requirement that the boundary condition on the body surface and the boundary conditions on the free surface match at the jet tip provides the constant, which appears upon integration of Equation (31) with $\sigma_0 = 1$; (3) in the present problem the forcing comes from the condition at infinity, while in the wedge-entry problem it comes from the body boundary condition; (4) the value $\sigma_0 = 1$ corresponds to the deadrise angle $\gamma = \pi/2$, which means that the wedge is just a vertical plate.

It should be noted that the solution of the inner boundary-value problem predicts unbounded velocities of the flow as $Vt/h_0 \to 0$. In order to resolve this singularity, the corresponding compressible solution has to be obtained for the very initial stage, when $c_0 t/h_0 = O(1)$ and matched to the solution of the inner problem (27) as $c_0 t/h_0 \to \infty$ but $Vt/h_0 \to 0$ [16].

A numerical approach aimed at solving the boundary-value problem for the inner flow and determining the self-similar solution is presented in Section 7. In the following, some features of the inner solution in the far-field and in the jet region are investigated through asymptotic analysis. Apart from providing useful insight into the characteristics of the solution, the knowledge of its asymptotic behavior in the far-field and in the jet region allows us to develop an efficient numerical algorithm and significantly reduce the size of the computational domain.

5. Asymptotic behavior of the inner solution in the far-field

The polar coordinates ρ, θ (Figure 2) are used below. In the far-field, $\rho \gg 1$, the shape of the free surface can be described by the equation $\theta = \tilde{\theta}(\rho)$, where $\tilde{\theta}(\rho) \to \beta$ as $\rho \to \infty$. The function $\tilde{\theta}(\rho)$ can be presented in the form

$$\tilde{\theta}(\rho) = \beta + \theta_1(\rho), \quad \theta_1(\rho) \to 0 \text{ as } \rho \to \infty\,. \tag{34}$$

It is required to determine the asymptotic behavior of the solution of the boundary-value problem (29–33) and the asymptotics of the function $\theta_1(\rho)$ as $\rho \to \infty$. The radial coordinate ρ is considered here as a large parameter. The far-field asymptotics of the functions $S(\rho, \theta)$ and $\theta_1(\rho)$ are not easy to find because $S(\rho, \theta)$ is defined in the region, the shape of which depends on the unknown function $\theta_1(\rho)$. It can be shown that the Stokes procedure, which is traditionally used in such cases, does not work for this particular problem. This is why we

suggest to map the far-field part of the inner flow region into a wedge-shaped region using the relation

$$\alpha = \theta \frac{\beta}{\tilde{\theta}(\rho)} \tag{35}$$

and introduce the new unknown function $\overline{S}(\rho, \alpha)$ by the equation

$$\overline{S}(\rho, \alpha) = \overline{S}\left(\rho, \theta \frac{\beta}{\tilde{\theta}(\rho)}\right) = S(\rho, \theta)\ . \tag{36}$$

The function $\overline{S}(\alpha, \rho)$ is defined in the region $0 < \alpha < \beta,\ \rho \gg 1$, whose shape does not already depend on the large parameter ρ.

As a drawback of the simpler shape of the fluid domain, the Poisson equation (29) and the boundary conditions (30) and (31) take more complicated forms. Using (34) and the formula $\mathrm{d}\tau = \sqrt{1 + \rho^2 \tilde{\theta}_\rho^2}\,\mathrm{d}\rho$, we can rewrite the dynamic boundary condition (31) as

$$\frac{\overline{S}_\rho^2}{1 + \rho^2 \tilde{\theta}_\rho^2} + 2\sigma_0 \overline{S} = (1 - \sigma_0)\rho^2 \quad (\alpha = \beta,\ \rho \gg 1), \tag{37}$$

while, in polar coordinates, the kinematic boundary condition on the free surface (30) leads to

$$S_\theta = \rho^2 \tilde{\theta}_\rho S_\rho \quad \text{on} \quad \theta = \tilde{\theta}(\rho).$$

By using Equations (34) and (35), we can present the kinematic boundary condition as

$$\frac{\mathrm{d}\tilde{\theta}}{\mathrm{d}\rho} = \frac{\beta \overline{S}_\alpha(\rho, \beta)[1 + \rho^2 \tilde{\theta}_\rho^2]}{\rho^2 \tilde{\theta}(\rho) \overline{S}_\rho(\rho, \beta)} \tag{38}$$

which is suitable for asymptotic analysis of the free-surface shape in the far-field.

In terms of the new variables ρ and α, the boundary condition on the body contour, $S_\theta(\rho, 0) = 0$ provides

$$\frac{\partial \overline{S}}{\partial \alpha} = 0 \quad (\alpha = 0,\ \ \rho \gg 1) \tag{39}$$

while the far-field condition (33) changes as follows

$$\overline{S} \sim -\frac{1}{2}\rho^2 - \rho^{\sigma_0} \cos(\sigma_0 \alpha) \quad (\rho \to \infty). \tag{40}$$

The Poisson equation (29)

$$S_{\rho\rho} + \frac{1}{\rho} S_\rho + \frac{1}{\rho^2} S_{\theta\theta} = -2$$

also changes due to the transformation of variables. Using Equations (34) and (35), we obtain

$$\overline{S}_{\rho\rho} + \frac{1}{\rho}\overline{S}_\rho + \frac{1}{\rho^2}\overline{S}_{\alpha\alpha} = -2 + U(\rho, \alpha) \quad (0 < \alpha < \beta,\ \ \rho \gg 1), \tag{41}$$

where

$$U(\rho, \alpha) = -2\overline{S}_{\rho\alpha}\alpha_\rho - \overline{S}_{\alpha\alpha}\alpha_\rho^2 - \overline{S}_\alpha \alpha_{\rho\rho} - \rho^{-1}\alpha_\rho \overline{S}_\alpha + \rho^{-2}\left[1 - (\beta/\tilde{\theta})^2\right]\overline{S}_{\alpha\alpha}$$

with α_ρ and $\alpha_{\rho\rho}$ given as

$$\alpha_\rho = -\alpha\tilde{\theta}_\rho/\tilde{\theta}(\rho), \qquad \alpha_{\rho\rho} = \alpha[2\tilde{\theta}_\rho^2 - \tilde{\theta}\tilde{\theta}_{\rho\rho}]/\tilde{\theta}^2(\rho).$$

The boundary-value problem (37–41) is solved by the method of successive approximations. Condition (40) implies that in the far-field the function $\overline{S}(\rho,\alpha)$ has the form

$$\overline{S}(\rho,\alpha) = -\frac{1}{2}\rho^2 - \rho^{\sigma_0}\cos(\sigma_0\alpha) + \overline{S}_1(\rho,\alpha), \tag{42}$$

where $\overline{S}_1(\rho,\alpha)\rho^{-\sigma_0} \to 0$ as $\rho \to \infty$. Substituting the representations of the unknown functions (34) and (42) in (37–41) and taking the leading-order terms, we obtain

$$\frac{\mathrm{d}\theta_1}{\mathrm{d}\rho} = -\sigma_0\rho^{\sigma_0-3}[1+o(1)], \tag{43}$$

from which we have

$$\theta_1(\rho) = \frac{\sigma_0}{2-\sigma_0}\rho^{\sigma_0-2} + \theta_2(\rho). \tag{44}$$

In terms of $\overline{S}_1$ the Poisson equation reads

$$\overline{S}_{1\rho\rho} + \frac{1}{\rho}\overline{S}_{1\rho} + \frac{1}{\rho^2}\overline{S}_{1\alpha\alpha} = \frac{\sigma_0^2}{\beta}\left[(2-3\sigma_0)\alpha\sin(\sigma_0\alpha) + \frac{2\sigma_0}{2-\sigma_0}\cos(\sigma_0\alpha)\right] \times \rho^{2\sigma_0-4}[1+o(1)], \quad (0<\alpha<\beta,\ \rho\gg 1), \tag{45}$$

while the dynamic boundary condition with account for the asymptotic behavior (43), gives

$$-2\rho\overline{S}_{1\rho} + 2\sigma_0\overline{S}_1 = \sigma_0^2\rho^{2\sigma_0-2}[1+o(1)] \quad (\alpha=\beta,\ \rho\gg 1),$$

yielding

$$\overline{S}_1(\rho,\beta) = \frac{\sigma_0^2}{2(2-\sigma_0)}\rho^{2\sigma_0-2} + \overline{S}_2(\rho,\beta), \tag{46}$$

where $\overline{S}_2(\rho,\beta)$ represents a higher-order contribution, $\overline{S}_2(\rho,\beta)\rho^{2-2\sigma_0} \to 0$ as $\rho \to \infty$.

The solution of the boundary-value problem (45), (46) along with the kinematic boundary condition and the condition along the body contour is sought in the form

$$\overline{S}_1(\rho,\alpha) = M(\alpha)\rho^{2\sigma_0-2} + \overline{S}_2(\rho,\alpha) \quad (0<\alpha<\beta). \tag{47}$$

It is worth noticing that this problem admits the eigensolution

$$\overline{S}_{1E}(\rho,\alpha) = C_1\rho^{-\sigma_0}\cos(\sigma_0\alpha), \tag{48}$$

which should be added to the particular solution (47). However, eigensolution (48) can be neglected in comparison with the term $M(\alpha)\rho^{2\sigma_0-2}$ in (47) as long as $2\sigma_0 - 2 > -\sigma_0$, that is $\sigma_0 > 2/3$ and $\gamma > \pi/4$. This case is considered first.

Substituting (47) in Equation (45) and retaining the leading-order terms, one gets the ordinary differential equation

$$M_{\alpha\alpha} + 4(1-\sigma_0)^2 M = \frac{1}{\beta}\sigma_0^2(2-3\sigma_0)\alpha\sin(\sigma_0\alpha) + \frac{2}{\beta}\frac{\sigma_0^3}{2-\sigma_0}\cos(\sigma_0\alpha), \quad (0<\alpha<\beta) \tag{49}$$

with the boundary conditions

$$M_\alpha(0)=0, \quad M(\beta)=\frac{\sigma_0^2}{2(2-\sigma_0)}. \tag{50}$$

Therefore

$$M(\alpha)=\frac{\sigma_0^2}{(2-\sigma_0)}\left\{\frac{\alpha}{\beta}\sin(\sigma_0\alpha)+\frac{\cos[2(1-\sigma_0)\alpha]}{2\cos(2\gamma)}\right\} \quad (0<\alpha<\beta),$$

that is

$$\overline{S}(\rho,\alpha)=-\frac{1}{2}\rho^2-\rho^{\sigma_0}\cos(\sigma_0\alpha)+\frac{\sigma_0^2}{(2-\sigma_0)}\left\{\frac{\alpha}{\beta}\sin(\sigma_0\alpha)+\frac{\cos[2(1-\sigma_0)\alpha]}{2\cos(2\gamma)}\right\}\rho^{2\sigma_0-2} + \overline{S}_2(\rho,\alpha). \tag{51}$$

As the next step, the representations (44) and (51) are substituted in the kinematic and dynamic boundary conditions; taking the leading order as $\rho\to\infty$, we obtain

$$\tilde{\theta}(\rho)=\beta+\frac{\sigma_0}{2-\sigma_0}\rho^{\sigma_0-2}-\frac{\sigma_0^2(1-\sigma_0)}{2(2-\sigma_0)^2}\tan(2\gamma)\rho^{2\sigma_0-4}+\theta_3(\rho). \tag{52}$$

$$\overline{S}(\rho,\beta)=-\frac{1}{2}\rho^2+\frac{\sigma_0^2}{2(2-\sigma_0)}\rho^{2\sigma_0-2}-\frac{\sigma_0^3(1-\sigma_0)}{2(2-\sigma_0)^2}\tan(2\gamma)\rho^{3\sigma_0-4}+\overline{S}_3(\rho,\beta), \tag{53}$$

where $\theta_3(\rho)\rho^{4-2\sigma_0}\to 0$ and $\overline{S}_3(\rho,\beta)\rho^{4-3\sigma_0}\to 0$ as $\rho\to\infty$. The asymptotic behavior of the function $\overline{S}_2(\rho,\alpha)$ is not considered here. It can be shown that the far-field asymptotics of the free-surface shape as given by Equation (52) corresponds to the asymptotics of the outer solution (15) near the intersection point.

A similar procedure can also be used for deadrise angles smaller that $\pi/4$. However, in this case the eigensolution (48) is no longer negligible and the asymptotic formula (47) has to be modified as

$$\overline{S}_1(\rho,\alpha)=C_1\rho^{-\sigma_0}\cos(\sigma_0\alpha)+M_1(\alpha)\rho^{2\sigma_0-2}+\overline{S}_2(\rho,\alpha).$$

After manipulations which are not represented here, in the case $\gamma<\pi/4$ we obtain

$$\overline{S}(\rho,\alpha)=-\frac{1}{2}\rho^2-\rho^{\sigma_0}\cos(\sigma_0\alpha)+C_1\rho^{-\sigma_0}\cos(\sigma_0\alpha) + \frac{\sigma_0^2}{(2-\sigma_0)}\left\{\frac{\alpha}{\beta}\sin(\sigma_0\alpha)+\frac{\cos[2(1-\sigma_0)\alpha]}{2\cos(2\gamma)}\right\}\rho^{2\sigma_0-2}[1+o(1)], \tag{54}$$

$$\tilde{\theta}(\rho)=\beta+\frac{\sigma_0}{2-\sigma_0}\rho^{\sigma_0-2}-\frac{\sigma_0C_1}{2+\sigma_0}\rho^{-(\sigma_0+2)}-\frac{\sigma_0^2(1-\sigma_0)}{2(2-\sigma_0)^2}\tan(2\gamma)\rho^{2\sigma_0-4}+\theta_3(\rho). \tag{55}$$

Correspondingly, from the dynamic boundary condition, it follows

$$\overline{S}(\rho,\beta)=-\frac{1}{2}\rho^2+\frac{\sigma_0^2}{2(2-\sigma_0)}\rho^{2\sigma_0-2}-\frac{\sigma_0^2C_1}{2+\sigma_0}\rho^{-2}-\frac{\sigma_0^3(1-\sigma_0)}{2(2-\sigma_0)^2}\tan(2\gamma)\rho^{3\sigma_0-4}+\overline{S}_3(\rho,\beta). \tag{56}$$

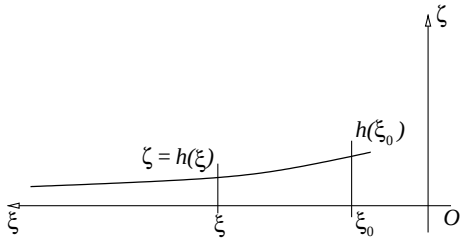

Figure 3. Local frame of reference used to derive asymptotic solution in the jet region.

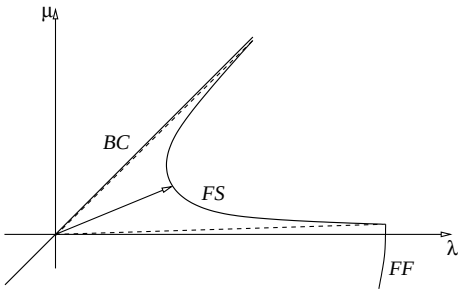

Figure 4. Sketch of the jet flow developing about the intersection point. From the mass-conservation law it follows that the area enclosed by the free surface and the two dashed lines should be equal to the flow coming in from the far-field boundary.

The case $\gamma=\pi/4$ requires a particular procedure as the eigensolution and the first term in (47) are of the same order. In this case $\sigma_0=2/3$ and it follows that

$$\overline{S}(\rho,\alpha)=-\frac{1}{2}\rho^2-\rho^{\frac{2}{3}}\cos\left(\frac{2}{3}\alpha\right)+\left[\frac{2}{9\pi}\alpha\sin\left(\frac{2}{3}\alpha\right)+\left(C_1-\frac{2}{9\pi}\log\rho\right)\cos\left(\frac{2}{3}\alpha\right)\right]\rho^{-\frac{2}{3}}+\overline{S}_2(\rho,\alpha), \tag{57}$$

$$\tilde{\theta}(\rho)=\beta+\frac{1}{2}\rho^{-\frac{4}{3}}+\frac{1}{18\pi}\rho^{-\frac{8}{3}}\log\rho-\left(\frac{1}{16\pi}+\frac{1}{4}C_1\right)\rho^{-\frac{8}{3}}+\theta_3(\rho), \tag{58}$$

$$\overline{S}(\rho,\beta)=-\frac{1}{2}\rho^2+\frac{1}{6}\rho^{-\frac{2}{3}}+\frac{1}{27\pi}\rho^{-2}\log\rho-\left(\frac{1}{24\pi}+\frac{1}{6}C_1\right)\rho^{-2}+\overline{S}_3(\rho,\beta). \tag{59}$$

The constant C_1 in (54–56) and in (57–59) is unknown in advance and has to be recovered together with the complete solution of the inner problem.

6. Asymptotic behavior of the flow in the jet region

Close to the wedge surface, the inner solution exhibits a jet formation whose asymptotic behavior can be investigated with the help of a shallow-water approximation. To this end a local coordinate system $O\xi\zeta$ is introduced with the axis $O\xi$ directed along the wedge surface and the free surface described by the equation $\zeta=h(\xi)$ (see Figure 3). The modified velocity potential on the free surface is written as $\tilde{S}(\xi)=S(\xi,h(\xi))$, with the function $h(\xi)$, $\xi>\xi_0$, which is unknown in advance and has to be determined as a part of the solution.

Within the new coordinate system the dynamic boundary condition (31) on the free surface takes the form

$$\frac{\tilde{S}_\xi^2}{1+h_\xi^2}+2\sigma_0\tilde{S}=(1-\sigma_0)\left(\xi^2+h^2(\xi)\right), \tag{60}$$

and the kinematic condition (30) gives

$$S_\zeta=h_\xi S_\xi. \tag{61}$$

The integration of the Poisson equation (29) in the ζ direction yields

$$\frac{\mathrm{d}}{\mathrm{d}\xi}\int_0^{h(\xi)} S_\xi(\xi,\zeta)\mathrm{d}\zeta - S_\xi(\xi,h(\xi))h_\xi + S_\zeta(\xi,h(\xi)) - S_\zeta(\xi,0) = -2h(\xi).$$

The second and the third terms on the left-hand side compensate each other due to (61), while the fourth term is zero due to the boundary condition on the body surface (32). Thus

$$\frac{\mathrm{d}}{\mathrm{d}\xi}\int_0^{h(\xi)} S_\xi(\xi,\zeta)\mathrm{d}\zeta = -2h(\xi). \tag{62}$$

Due to the boundary condition on the body surface, $S_\zeta(\xi,0)=0$, and since $h(\xi)\to 0$ as $\xi\to\infty$, the shallow-water approximation can be used. According to the shallow-water approximation we assume

$$S(\xi,\zeta)\approx\tilde{S}(\xi) \tag{63}$$

and Equation (62) yields

$$\left[\tilde{S}_\xi h\right]_\xi + 2h\approx 0. \tag{64}$$

Equations (60) and (64) can be used to evaluate approximately the free-surface shape in the jet region. For large ξ, when the derivative $h_\xi(\xi)$ is small, Equation (60) can be approximated as

$$\tilde{S}_\xi^2 \approx (1-\sigma_0)\xi^2 - 2\sigma_0\tilde{S}.$$

The solution of the latter equation has the form

$$\tilde{S}(\xi) = M\xi^2$$

with $M=1/2(1-\sigma_0)$ or $M=-1/2$. Substituting this solution in Equation (64), the following equation is obtained for the jet thickness

$$\xi h_\xi + \frac{M+1}{M}h\approx 0.$$

When $M=-\frac{1}{2}$, we find $h(\xi)\approx C\xi$, which contradicts the condition $h(\xi)\to 0$ as $\xi\to\infty$. When $M=\frac{1}{2}(1-\sigma_0)$, we obtain

$$h(\xi)\approx C\xi^{-b}, \quad b=\frac{3-\sigma_0}{1-\sigma_0}, \tag{65}$$

which gives $\xi h(\xi) = O(\xi^{-\frac{2}{1-\sigma_0}})$ as $\xi\to\infty$. Hence, as $\xi\to\infty$, the jet thickness tends to zero as $O(\xi^{-b})$, where b depends on the wedge deadrise angle γ, and the liquid velocity in the jet grows linearly

$$\varphi_\xi \sim (2-\sigma_0)\xi \quad \text{as } \xi\to\infty \tag{66}$$

with distance from the origin of the coordinate system. Therefore, the mass flux in the jet behaves as

$$\int_0^{h(\xi)} \frac{\partial\varphi}{\partial\xi}(\xi,\eta)\mathrm{d}\eta \sim C\xi^{-2/(1-\sigma_0)} \tag{67}$$

and tends to zero as $\xi\to\infty$.

Up to this point the shallow-water model has been developed within a first-order approximation. To improve accuracy, a second-order shallow-water model is derived in Appendix A and is coupled with the numerical procedure to describe the solution in the thin jet layer.

7. Numerical pseudo-time-stepping procedure

In Section 4 two different boundary-value problems have been formulated for the velocity potential φ, given by the set of Equations (27), and for the modified potential S, given by Equations (29–33). The former, involving the Laplace equation, is simpler but it has much more complex boundary conditions on the free surface. Hence, an iterative procedure is developed here which takes advantage of both boundary-value problems and uses Equation (28) to pass from the velocity potential to the modified one and vice versa.

The velocity potential φ is sought in terms of a boundary-integral representation in a computational domain bounded by the far-field boundary (FF) located at $\rho=\rho_F$, the body contour (BC) and the free surface (Figure 4). On the body contour, the Neumann boundary condition $\partial\varphi/\partial n=0$ is applied. On the free surface the modified velocity potential S is derived by integrating the dynamic boundary condition rewritten in the form

$$S_\tau=-\sqrt{(1-\sigma_0)\rho^2-2\sigma_0 S}. \tag{68}$$

Integration is started from the intersection of the free surface with the far-field boundary where the modified velocity potential is provided by the far-field asymptotics. The position of the intersection point $\tilde{\theta}(\rho_F)$ is given by Equations (52), (55) or (58) for γ larger, smaller or equal to $\pi/4$, respectively. Correspondingly, Equations (53), (56) or (59) are used to assign the starting value $S(\rho_F,\tilde{\theta}(\rho_F))$ and Equations (51), (54) or (57) are used to assign the modified velocity potential at the far-field boundary. Then, Equation (28) allows to derive φ from S. The radius of the far-field boundary is chosen such that the far-field asymptotics describe the solution to the desired accuracy for $\rho\geq\rho_F$. The far-field asymptotic estimate is also used to derive a first guess for the free-surface shape.

In order to avoid the intrinsic limit that boundary-element approaches have in describing the solution within layers of thickness comparable to the panel size, the shallow-water model is adopted to derive the solution in the thinner part of the jet. This part is not distinguished during several iterations at the beginning. However, as the iterations proceed, the thin jet develops and the angle at the intersection between the free surface and the body contour progressively decays. When it becomes smaller than a threshold value, the shallow-water model is activated and integrated into the boundary-integral representation. The details of the space marching procedure used to derive the shallow-water solution are reported at the end of Appendix A. For the purpose of this section, it is useful to recall that the shallow-water model provides the free-surface shape, the velocity potential and its normal derivative along the jet contour.

On the basis of the above considerations, when writing the boundary-integral representation of the velocity potential, the contributions to the integrals of the part of the fluid boundary lying inside the shallow-water region SW are treated as known terms, and the boundary-integral equation reads

$$\begin{aligned}\frac{1}{2}\varphi(\boldsymbol{x})+\int_{BC}\varphi(\boldsymbol{y})\frac{\partial G}{\partial n}(\boldsymbol{x}-\boldsymbol{y})\mathrm{d}s(\boldsymbol{y})-\int_{FS\cup FF}\frac{\partial\varphi}{\partial n}(\boldsymbol{y})G(\boldsymbol{x}-\boldsymbol{y})\mathrm{d}s(\boldsymbol{y})\\ =\int_{BC\cup SW}\frac{\partial\varphi}{\partial n}(\boldsymbol{y})G(\boldsymbol{x}-\boldsymbol{y})\mathrm{d}s(\boldsymbol{y})-\int_{FS\cup FF\cup SW}\varphi(\boldsymbol{y})\frac{\partial G}{\partial n}(\boldsymbol{x}-\boldsymbol{y})\mathrm{d}s(\boldsymbol{y}),\end{aligned} \tag{69}$$

where FS denotes the portion of the free surface outside the modeled part of the jet. Here $G(\mathbf{x})=\frac{1}{2\pi}\log|\mathbf{x}|$ is the Green's function of the Laplace equation and $\mathbf{x}=(\lambda,\mu)$. The first term on the left-hand side is known at any point of both the free surface and the far-field boundary and is then moved to the right part when $\mathbf{x}\in FF\cup FS$. The right-hand side of Equation (69) is known at each step of the iterations with the first term being zero along the body

contour due to the condition $\partial\varphi/\partial n = 0$ and the velocity potential on the far-field boundary assigned by the far-field asymptotics, as discussed above.

The solution of the boundary-integral equation is achieved through a panel method. The boundary of the computational domain is discretized with straight-line panels, along which a constant value of the velocity potential and of its normal derivative are assumed. Once Equation (69) has been solved, the distribution of the normal derivative of the velocity potential $\partial\varphi/\partial n$ on the free surface is obtained and used to compute $\partial S/\partial n$. After that we verify if the kinematic boundary condition on the free surface, as given by Equation (30), is satisfied to the desired accuracy. If not, the centroids of the panels are moved in a time-stepping fashion by using ∇S as the velocity field. Then we reconstruct the distribution of the vertices of the panels with the help of cubic splines.

In order to preserve the accuracy of the calculation, the discretization is refined at each iteration. In particular, the size of the first free-surface panel closest to the jet is progressively adjusted so as to be of the order of the local thickness of the jet. Starting from this value, a growth factor for the panel size is used up to completely fill the free-surface configuration; a similar procedure is used to discretize the body contour. To avoid the occurrence of panels that are too short, the smallest size is limited to a fraction of the initial size of the free-surface panel closest to the body. Once the free-surface discretization is updated, the dynamic boundary condition (68) is integrated along it to obtain, as discussed before, the velocity potential along the free surface and the integral equation (69) is solved once again.

The iterative procedure continues until the kinematic condition (30) is satisfied at a desired accuracy. To this end the integral

$$\mathcal{K} = \int_{FS} \left(\frac{\partial S}{\partial n}(\mathbf{y}) \right)^2 \mathrm{d}s(\mathbf{y}) \tag{70}$$

is evaluated and iterations are repeated until $\mathcal{K}$ becomes smaller than a threshold value. Besides evaluating the quantity $\mathcal{K}$ given by Equation (70), the fulfillment of mass conservation is carefully analyzed. For incompressible fluids, it follows that

$$\int_{FF \cup FS} \frac{\partial \varphi}{\partial n} \, \mathrm{d}s = 0, \tag{71}$$

where, due to Equations (28) and (30),

$$\frac{\partial \varphi}{\partial n} = \rho \frac{\partial \rho}{\partial n}$$

along the free surface FS, so that

$$\int_{FF} \frac{\partial \varphi}{\partial n} \, \mathrm{d}s = -\int_{FS} \rho \frac{\partial \rho}{\partial n} \, \mathrm{d}s, \tag{72}$$

where the term on the right-hand side represents the area of the region swept by a vector connecting the origin with a point on the free surface when the point moves from the far-field to the jet apex (Figure 5). When the jet region is modeled within the shallow-water approximation, Equation (72) takes the form

$$\int_{FF} \frac{\partial \varphi}{\partial n} \, \mathrm{d}s = -\int_{FS \cup SW} \rho \frac{\partial \rho}{\partial n} \, \mathrm{d}s, \tag{73}$$

where

$$\int_{SW} \rho \left(\frac{\partial \rho}{\partial n} \right) \mathrm{d}s = 2 \int_{\xi_0}^{\infty} h(\xi) \, \mathrm{d}\xi + \xi_0 h(\xi_0),$$

with $h(\xi) = h(\xi_0) H_0(\xi)$, as it follows from the definition (A1).

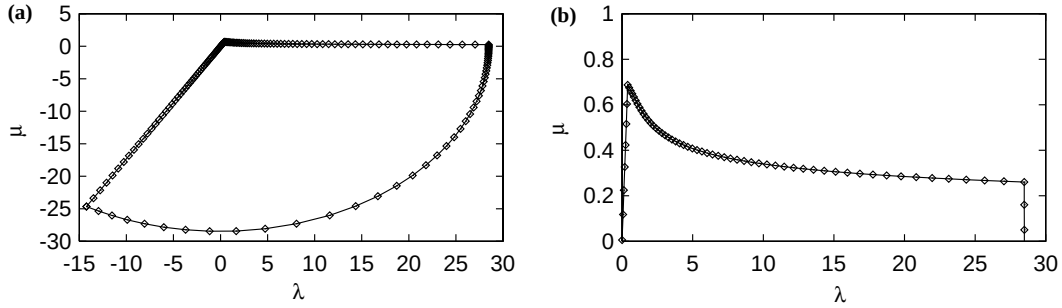

Figure 5. The computational domain and the discretization of its boundary employed at the first iteration are here shown. (*a*) the whole computational domain, (*b*) detail of the free surface discretization.

For deadrise angles equal or smaller than $\pi/4$ the modified velocity potential and the free-surface shape given by the far-field asymptotics contain an undetermined constant C_1 which must be evaluated together with the solution in the intermediate region. To this end the far-field expansions are recast in a way that represents the velocity potential and its normal derivative as the sums of two contributions

$$\varphi \approx \varphi_0 + C_1\varphi_1, \quad \frac{\partial\varphi}{\partial n} \approx \frac{\partial\varphi_0}{\partial n} + C_1\frac{\partial\varphi_1}{\partial n}, \tag{74}$$

where subscript 1 denotes the eigensolution parts. By using expressions (74) in the boundary-integral equation (69) we obtain

$$\begin{aligned}\frac{1}{2}\varphi(\boldsymbol{x}) + \int_{BC}\varphi(\boldsymbol{y})\frac{\partial G}{\partial n}(\boldsymbol{x}-\boldsymbol{y})\mathrm{d}s(\boldsymbol{y}) - \int_{FS\cup FF}\frac{\partial\varphi}{\partial n}(\boldsymbol{y})G(\boldsymbol{x}-\boldsymbol{y})\mathrm{d}s(\boldsymbol{y}) \\ + C_1\int_{FF}\varphi_1(\boldsymbol{y})\frac{\partial G}{\partial n}(\boldsymbol{x}-\boldsymbol{y})\mathrm{d}s(\boldsymbol{y}) = \int_{BC\cup SW}\frac{\partial\varphi}{\partial n}(\boldsymbol{y})G(\boldsymbol{x}-\boldsymbol{y})\mathrm{d}s(\boldsymbol{y}) \\ - \int_{FS\cup SW}\varphi(\boldsymbol{y})\frac{\partial G}{\partial n}(\boldsymbol{x}-\boldsymbol{y})\mathrm{d}s(\boldsymbol{y}) - \int_{FF}\varphi_0(\boldsymbol{y})\frac{\partial G}{\partial n}(\boldsymbol{x}-\boldsymbol{y})\mathrm{d}s(\boldsymbol{y}).\end{aligned} \tag{75}$$

The additional equation needed to close the linear system of Equation (75) is obtained by requiring that the flow coming in from the far-field boundary must be equal to the sum of the two contributions from φ_0 and φ_1, that is,

$$-\int_{FF}\frac{\partial\varphi}{\partial n}\mathrm{d}s + C_1\int_{FF}\frac{\partial\varphi_1}{\partial n}\mathrm{d}s = -\int_{FF}\frac{\partial\varphi_0}{\partial n}\mathrm{d}s. \tag{76}$$

Once the linear system (75) with Equation (76) is solved, the constant C_1 is used at the next iteration to update the position of the intersection between the free surface and the far-field boundary by Equations (55) or (58) depending on $\gamma < \pi/4$ or $\gamma = \pi/4$, respectively. Next, the value of this constant is used in Equation (56) or (59) to compute the velocity potential at the last free-surface vertex and, then, to update the velocity potential all along the free surface.

8. Numerical results

The numerical model presented in the previous section is applied to derive the self-similar solution of the inner problem for deadrise angles larger ($\gamma = \pi/3$) and smaller ($\gamma = \pi/6$) than $\pi/4$. Since the asymptotic expansions derived in Section 5 are used outside the computational domain, that is, for $\rho > \rho_F$, the far-field radius ρ_F is assigned is such a way that

terms of order $O(\rho^{3\sigma_0-5})$ can be neglected in the expansions to within the desired accuracy for $\rho > \rho_F$. In the following calculations, the far-field radius has been chosen so that $\rho_F^{3\sigma_0-5} = 10^{-4}$. The initial size of the first panel on the free surface closest to the body is 0·1 and the smallest panel size is limited to 1/50 of this value. A growth factor 1·05 is used to increase the panel size to fill the free-surface shape. The shallow-water approximation is usually activated when the angle of the free surface with the body contour drops below 10 degrees.

In Figure 5*a*, *b* both the initial discretization and the computational domain are shown in the case $\gamma = \pi/3$ with $\rho_F \sim 28$. Figure 6 shows the distribution of $\partial S/\partial n$ along the initial guess of the free-surface position. The iterative procedure is started from this configuration and in Figure 7 the history of $\mathcal{K}$ versus the iteration number is depicted. Due to numerical approximations, the accuracy of the kinematic boundary condition does not go below a threshold value. However, a comparison between the solutions after 1500 and 3000 iterations shows that they essentially overlap in terms of both the free-surface shape (Figures 8*a*, *b*) and the modified velocity potential (Figure 9). There are two lines in Figure 9 but a difference between them is not visible. It is seen also that the function S on the free surface changes rather smoothly at the matching point between the intermediate region and the jet region. As the iterations continue, the enclosed area tends to the incoming flow (Figure 10) as required by Equation (73). Since $\partial\varphi/\partial n$ along the far-field boundary is unknown and is determined from the solution of the

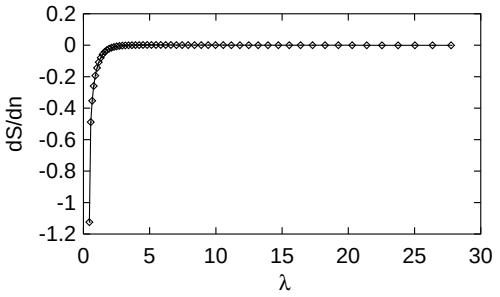

Figure 6. Distribution of the normal derivative of the modified velocity potential $\partial S/\partial n$ along the initial free-surface configuration.

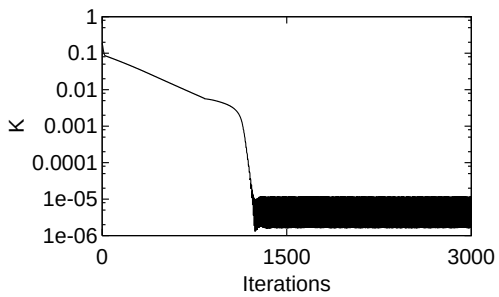

Figure 7. The quantity $\mathcal{K}$ versus the iteration number: convergence is essentially reached after about 1500 iterations, in the case $\gamma = \pi/3$.

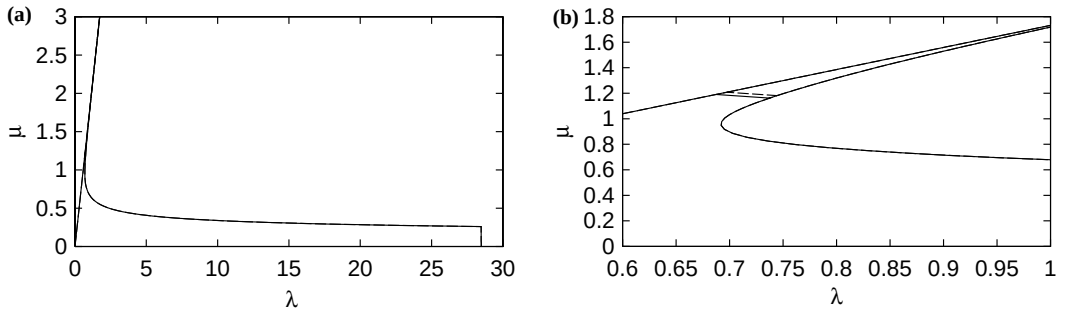

Figure 8. Free surface configuration at two different steps of the iterative procedure: (*a*) whole free surface; (*b*) close-up view of the jet region. The free surface shape after 1500 iterations is shown with the solid line and after 3000 iterations with the dashed line.

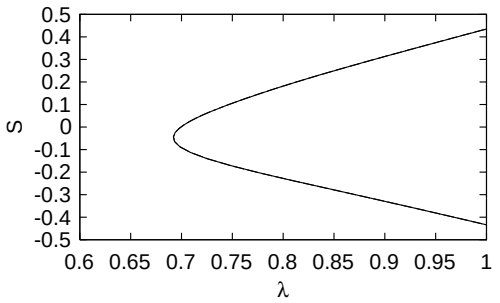

Figure 9. Distribution of the modified velocity potential about the matching point between the intermediate region and the jet region at two different steps. The matching point between the two regions is located at $\lambda \simeq 0{\cdot}75$ on the upper branch of the curve. The modified velocity potential after 1500 iterations is shown with the solid line and after 3000 iterations with the dashed line.

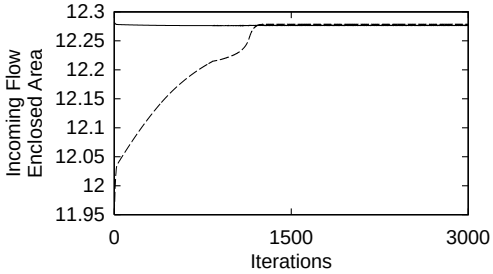

Figure 10. Comparison between the convergence histories of the flow incoming from the far-field boundary (solid line) and the area enclosed by the free surface (dashed line).

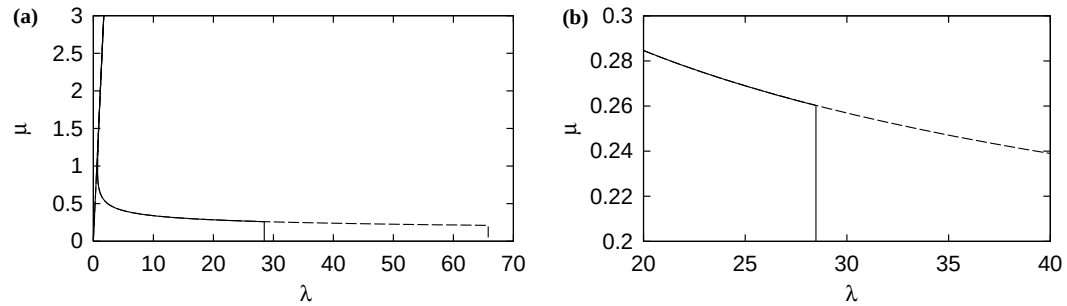

Figure 11. Effect of the extension of the computational domain on the final solution: (*a*) whole free surface; (*b*) detailed view of the region about the far-field boundary of the smallest domain. Key: small domain with $\rho_F \sim 28$ (solid line), large domain with $\rho_F \sim 66$ (dashed line).

boundary-integral-equation within the numerical procedure, the incoming flow slightly changes in time.

Several tests were carried out to check the independence of the solution of the extension of the computational domain (Figure 11*a*, *b*), of the limit angle used to cut the jet (Figures 12 and 13) and of the resolution employed (Figures 14*a*, *b* and 15). The tests proved stability and accuracy of the numerical algorithm developed.

In the case $\gamma = \pi/6$, the efficiency of the new formulation (75) and (76) presented at the end of the previous section, is investigated. Since the use of larger computational domains reduces the effect of the eigensolution part, three calculations are performed by using three different values of the radius ρ_F of the far-field boundary, with the eigensolution term only included for the smallest domain. In particular, the smallest radius is chosen so that $\rho_F^{3\sigma_0-5} \simeq 10^{-4}$, which leads to $\rho_F \simeq 18$. Correspondingly, other calculations are performed in larger computational domains with $\rho_F^{3\sigma_0-5} \simeq 10^{-5}, 10^{-6}$, that is $\rho_F \simeq 36$ and 75, respectively. In Figure 16*a* the behavior of these three solutions, close to the end of the shortest domain, is shown to highlight the role of the eigensolution term and the effectiveness of the formulation (75) and (76). It is worth noticing that an improvement of the accuracy is also achieved in the jet region (Figure 16*b*).

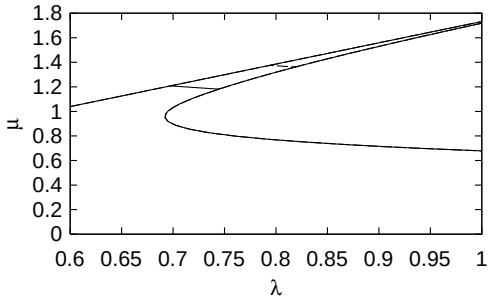

Figure 12. Effect of the limit angle for the activation of the shallow-water approximation on the final solution. Key: 10 degrees (solid line), 5 degrees (dashed line).

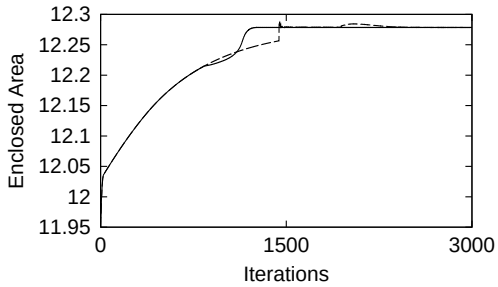

Figure 13. Comparison of the histories of the enclosed area versus the iteration number obtained when using different values of the limit angle to activate the shallow-water solution. Key: 10 degrees (solid line), 5 degrees (dashed line).

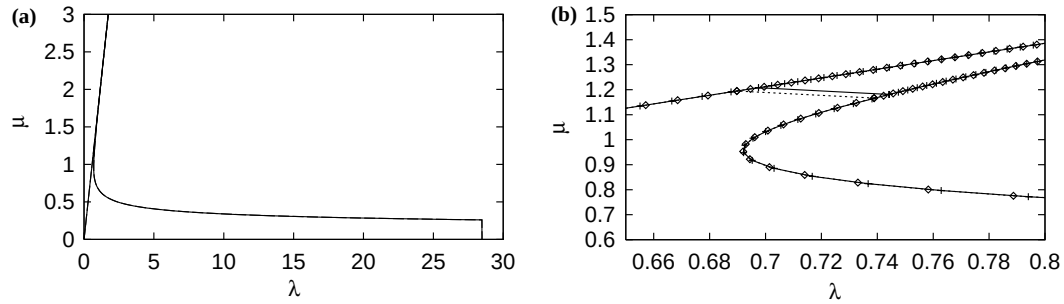

Figure 14. Effect of the initial discretization on the final solution. Comparison is established between solutions obtained when using different values of the initial size free-surface panel closest to the body: (*a*) whole free surface; (*b*) detailed view of the discretization in the jet region. Key: initial first panel size 0·4 (solid line), initial first panel size 0·1 (dashed line).

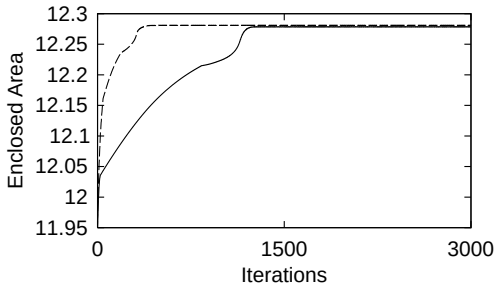

Figure 15. Comparison of the convergence histories of the enclosed area obtained when using different initial discretization. Key: initial first panel size 0·4 (solid line), initial first panel size 0·1 (dashed line).

In Figure 17 the behavior of the constant C_1 versus the iteration number and the pseudo-time has been plotted. In particular Figure 17*a* shows that the convergence of the constant versus the iteration number is not uniform, with an apparent convergence reached after about 1000 iterations and a successive, final, convergence achieved after about 2000 iterations.

The reason for this behavior stems from the use of a variable time step in the iterative procedure. In fact, for stability reasons the time step dt is adjusted so that the displacement of

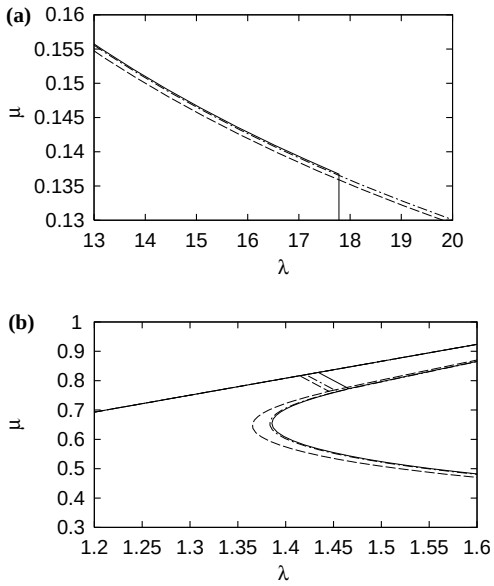

Figure 16. Comparison among solutions obtained for $\gamma = \pi/6$ by using three different extensions of the computational domain. Only for the smallest computational domain the new formulation (74–75) has been employed: (*a*) detailed view about the end of the smallest domain; (*b*) detailed view about the jet region. Key: $\rho_F \sim 18$ and new formulation (solid line), $\rho_F \sim 36$ (*dashed line*), $\rho_F \sim 75$ (dash-dotted line).

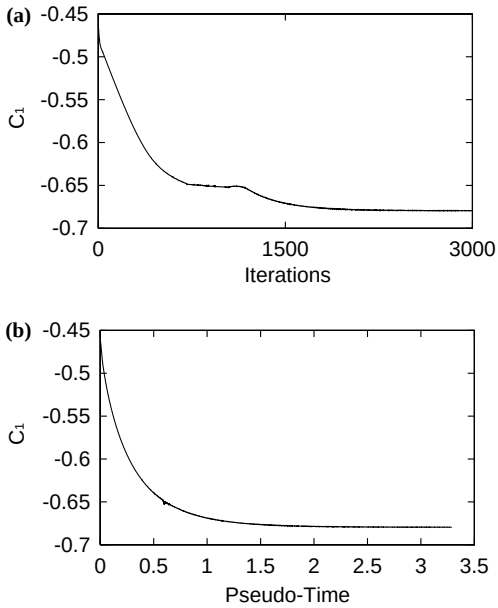

Figure 17. Convergence history of C_1 for $\gamma = \pi/6$ versus the iteration number (*a*) and the pseudo-time (*b*).

the panel centroid, which is $|\nabla S|\mathrm{d}t$, is always smaller than one fourth of the corresponding panel length. As a consequence, very small-time steps occur during the iterative process due to the occurrence of very short panels. This hypothesis is confirmed by looking at Figure 17*b*, where the same quantity is plotted versus the pseudo-time. In this case the convergence behavior appears to be remarkably uniform.

In Figure 18*a*, *b* the histories of the enclosed area and of the incoming flow are shown, versus the iteration number, for the smallest and the largest computational domains. It is seen how, apart from reducing the size of the computational domain needed, the use of (75) and (76) makes the convergence much faster. Also in this case the apparent non-uniform convergence of the enclosed area is a result of the very small-time steps occurring during the iterative process.

By using the same computational procedure, solutions for deadrise-angle values from 10 to 45 degrees are computed and the constant of the eigensolutions is reported in Table 1 and plotted in Figure 19 versus the deadrise angle value.

9. Conclusions

The initial stage of the free-surface flow generated by the impulsive start of a wedge initially floating on the free surface has been carefully analyzed through a small-time expansion procedure. Due to the singularity of the flow about the intersection points, a first-order inner solu-

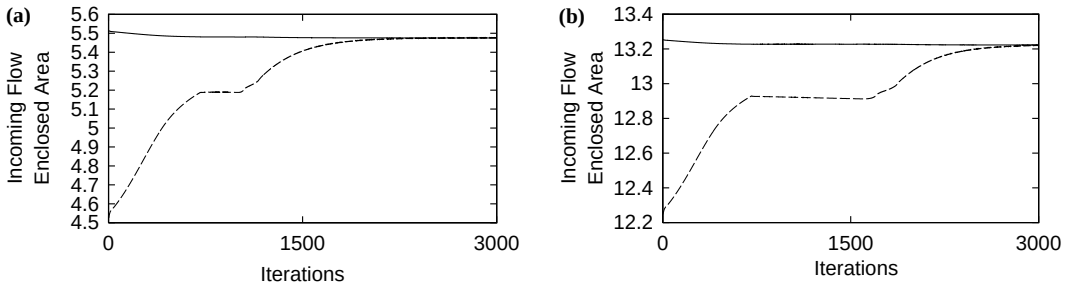

Figure 18. Comparison between the incoming flow and the enclosed area for $\gamma = \pi/6$: (*a*) smallest computational domain, $\rho_f \sim 18$, and the new formulation; (*b*) largest computational domain, $\rho_F \sim 75$. Key: incoming flow (solid line), enclosed area (dashed line).

Table 1. Constant of the eigensolution for several deadrise-angle-values.

γ	C_1
10	−1· 4630
15	−1· 0874
20	−0· 8862
25	−0· 7620
30	−0· 6795
35	−0· 6303
40	−0· 5998
45	−0· 5651

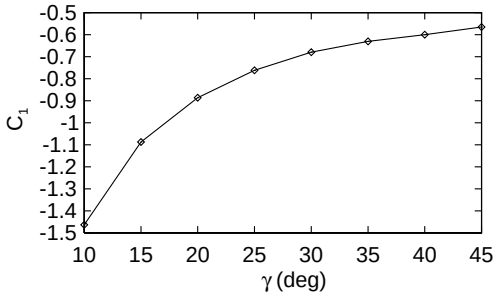

Figure 19. Plot of the constant of the eigensolution C_1 versus the deadrise angle. Corresponding values are reported in Table 1.

tion has been derived in terms of a suitable set of stretched variables. It is shown that, as long as $Vt/h_0 \to 0$, the inner solution is self-similar and nonlinear.

The system of partial differential equations governing the flow close to the intersection points has been used to derive asymptotic estimates of the flow behavior in both the far-field and the jet regions. The two asymptotic estimates are directly coupled with the numerical solver thus achieving a high efficiency in the iterative procedure. When dealing with deadrise angles equal to or smaller than $\pi/4$, eigensolutions have been found in the asymptotic estimate of the far-field behavior. For this case, the numerical model has been suitably modified in order to recover the eigenvalue directly as part of the solution.

The approach has been illustrated for two deadrise angles, $\pi/6$ and $\pi/3$, the former case being chosen to show the efficiency of the numerical approach for deriving the eigenvalue as part of the solution. It is worth remarking that for rather small deadrise angles the way used to define the set of inner variables cannot always ensure good accuracy but the approach developed by Oliver [9] on the base of the Wagner approximation should be employed instead.

The asymptotic behavior (14) of the first-order outer velocity potential close to the intersection point is not only a feature of the particular problem of floating-wedge impact. This asymptotic formula is valid also for any flared floating contour, with γ being the angle between the tangential to the contour at the intersection point and the initially undisturbed free surface and the coefficient A dependent on the body shape and on the entry velocity. With this consideration, the performed analysis of the local solution near the intersection point is also valid for any floating body with $0 < \gamma < \pi/2$.

It is expected that in the three-dimensional problem of floating body impact, where the body is smooth and flared, the asymptotic behavior of the outer potential near the intersection line is also described by Equation (14), which is valid at any point of the intersection line (see [17] for more details). Now γ is the local deadrise angle, the polar coordinates (r, θ) are in the vertical plane, which is locally normal to the body surface and the "constant" A in Equation (14) is a function of the coordinate along the intersection line. Therefore, the analysis presented in this paper has a much wider field of application than just for the plane problem of floating-wedge impact.

Acknowledgements

A.A.K. acknowledges the support from RFBR (projects No. 00-01-00839 and No. NS-902.2003.1). A.I. acknowledges the support from *Ministero dei Trasporti e Navigazione* in the framework of the INSEAN research plan 2000–2002. Preliminary results of this work were presented at the Fifteenth International Workshop on Water Waves and Floating Bodies, Caesarea, Israel, 27 February–01 March, 2000 and at the Sixteenth International Workshop on Water Waves and Floating Bodies, Hiroshima, Japan, 22–25 April, 2001.

Appendix A: Second-order shallow water approximation

In order to improve the accuracy in the description of the flow in the jet region, a second-order shallow-water approximation is derived here. To this end, we fix a positive ξ_0 and take the quantity $\varepsilon = h(\xi_0)$ as a small parameter (Figure 3). With this assumption the local thickness of the jet is sought in the form

$$h(\xi) = \varepsilon H(\xi), \tag{A.1}$$

where $H(\xi_0) = 1$ and $H(\xi) \le 1$ for $\xi > \xi_0$. In order to start the asymptotic analysis of the flow, the jet region is mapped onto the rectangular domain $0 < z < 1, \xi > \xi_0$ by the relation

$$\zeta = \varepsilon H(\xi) z, \tag{A.2}$$

and the new unknown function

$$s(\xi, z) = S(\xi, \varepsilon H(\xi) z) \tag{A.3}$$

is introduced to represent the modified velocity potential in the jet region. By using Equations (A.1–A.3), we obtain

$$S_{\xi\xi} = s_{\xi\xi} - 2z s_{\xi z} \frac{H_\xi}{H} + z s_z \left(\frac{H_\xi}{H}\right)^2 + z^2 s_{zz} \left(\frac{H_\xi}{H}\right)^2 - z s_z \left(\frac{H_\xi}{H}\right)_\xi, \; S_{\zeta\zeta} = s_{zz} \left(\frac{1}{\varepsilon H}\right)^2.$$

The Poisson equation (29) can be rewritten in the new variables as

$$s_{zz}\left[1 + \varepsilon^2 z^2 H_\xi^2\right] + \varepsilon^2 \left[H^2 s_{\xi\xi} - 2z H H_\xi s_{\xi z} + z H_\xi^2 s_z - z\left(H_{\xi\xi} H - H_\xi^2\right) s_z\right] = -2\varepsilon^2 H^2, \quad (0 < z < 1, \xi > \xi_0). \tag{A.4}$$

The kinematic boundary condition (30) implies that $S_\zeta = h_\xi S_\xi$ on the free surface $z = 1$, which leads to

$$s_z = \varepsilon^2 H_\xi \left(H s_\xi - z s_z H_\xi\right) \quad (z = 1, \xi > \xi_0), \tag{A.5}$$

while the body boundary condition (32) provides

$$s_z = 0 \quad (z = 0\,,\, \xi > \xi_0). \tag{A.6}$$

The dynamic boundary condition (31), which in terms of the new variables takes the form

$$\frac{\tilde{S}_\xi^2}{(1+h_\xi^2)} + 2\sigma_0 \tilde{S} = (\xi^2 + h^2)(1-\sigma_0) \quad (\xi > \xi_0),$$

with $\tilde{S}(\xi) = S(\xi, h(\xi)) = s(\xi, 1)$, gives

$$s_\xi^2 = \left[(1-\sigma_0)\left(\xi^2 + \varepsilon^2 H^2\right) - 2\sigma_0 s\right](1 + \varepsilon^2 H_\xi^2) \quad (z = 1, \xi > \xi_0). \tag{A.7}$$

We assume that at $\xi = \xi_0$ on the free surface, the matching with the numerical solution of the boundary-value problem (29–33) is enforced in terms of jet thickness $h(\xi_0) = h_0$ and modified velocity potential $S(\xi_0, \varepsilon) = S_0$. Therefore

$$s(\xi_0, 1) = S_0, \tag{A.8}$$

and from the first-order approximation we have that

$$s(\xi, z) \sim \frac{1}{2}(1-\sigma_0)\xi^2 \quad (\xi \to \infty). \tag{A.9}$$

The boundary-value problem (A.4–A.9) contains the small parameter ε. The solution of the problem is sought in the form of the asymptotic expansions

$$s(\xi, z) = s_0(\xi, z) + \varepsilon^2 s_1(\xi, z) + \varepsilon^4 s_2(\xi, z) + \cdots, \tag{A.10}$$

$$H(\xi) = H_0(\xi) + \varepsilon^2 H_1(\xi) + \varepsilon^4 H_2(\xi) + \cdots. \tag{A.11}$$

We shall derive equations which govern the second-order solution of the flow in the jet region.

Substituting expansions (A.10) and (A.11) in the governing equations (A.4–A.9) and collecting terms of the same order as $\varepsilon \to 0$, we obtain a boundary-value problems for the unknown functions $s_j(\xi, z)$ and $H_j(\xi)$. At the leading order the Poisson equation (A.4) reads

$$s_{0zz} = 0 \quad (0 < z < 1) \tag{A.12}$$

while the kinematic condition (A.5) and the body boundary condition (A.6) give

$$s_{0z} = 0 \quad (z = 0, 1). \tag{A.13}$$

Equations (A.12) and (A.13) imply that s_0 only depends on ξ and can be found with the help of the dynamic boundary condition (A.7) which, at the leading order, provides

$$s_{0\xi}^2 + 2\sigma_0 s_0 = (1-\sigma_0)\xi^2. \tag{A.14}$$

The general solution of the differential equation (A.14), with account for condition (A.9), is sought in the form

$$s_0(\xi) = \xi^2 k(\omega), \quad \omega = \log \xi, \tag{A.15}$$

where $k(\omega) \to \frac{1}{2}(1-\sigma_0)$ as $\omega \to \infty$. Substituting (A.15) in (A.14), we obtain

$$\frac{\mathrm{d}k}{\mathrm{d}\omega} = \sqrt{1 - \sigma_0 - 2\sigma_0 k} - 2k. \tag{A.16}$$

By introducing a new function $v=\sqrt{1-\sigma_0-2\sigma_0 k}$, it follows that

$$k=\frac{1-\sigma_0}{2\sigma_0}-\frac{v^2}{2\sigma_0}$$

which, after differentiation with respect to ω, provides

$$\frac{\mathrm{d}k}{\mathrm{d}\omega}=-\frac{v}{\sigma_0}\frac{\mathrm{d}v}{\mathrm{d}\omega}. \tag{A.17}$$

Combining Equations (A.16) and (A.17), we obtain

$$\frac{v}{v^2+\sigma_0 v+\sigma_0-1}\mathrm{d}v=-\mathrm{d}\omega,$$

whose integration leads to the equation

$$v(\xi)=1-\sigma_0+D\xi^{-(2-\sigma_0)/(1-\sigma_0)}(1+v)^{-1/(1-\sigma_0)} \tag{A.18}$$

with an arbitrary constant D. In order to recover the relation between v and the modified velocity potential s_0, the definitions of k and v can be used to get

$$v^2\xi^2=(1-\sigma_0)\xi^2-2\sigma_0 s_0, \tag{A.19}$$

which, together with the dynamic boundary condition (A.14), gives

$$s_{0\xi}=\xi v. \tag{A.20}$$

The constant D in (A.18) is determined numerically with the help of condition (A.8) at $\xi=\xi_0$, which gives $s_0(\xi_0)=S_0$, and Equations (A.18) and (A.20). Equations (A.18) and (A.19) completely determine the velocity potential to leading order.

Within the second-order, the Poisson equation (A.4) gives

$$s_{1zz}=-2H_0^2-H_0^2 s_{0\xi\xi} \tag{A.21}$$

whose solution has to satisfy the boundary condition on the body $s_{1z}=0$, where $z=0$, and the kinematic and dynamic boundary conditions on the free surface, $z=1$, that read

$$s_{1z}=H_{0\xi}H_0 s_{0\xi} \tag{A.22}$$

and

$$2s_{0\xi}s_{1\xi}=(1-\sigma_0)H_0^2-2\sigma_0 s_1+H_{0\xi}^2[(1-\sigma_0)\xi^2-2\sigma_0 s_0], \tag{A.23}$$

respectively. The general solution of Equation (A.21) has the form

$$s_1(\xi,z)=-\frac{z^2}{2}\left[2H_0^2+H_0^2 s_{0\xi\xi}\right]+B(\xi), \tag{A.24}$$

which already accounts for the body boundary condition. The function $B(\xi)$ in (A.24) is determined from the dynamic boundary condition (A.23), where $H_0(\xi)$ is still unknown.

The kinematic boundary condition (A.22) and representation (A.24) lead to the following differential equation with respect to this function

$$\frac{\mathrm{d}}{\mathrm{d}\xi}\left(H_0 s_{0\xi}\right)=-2H_0 \quad (\xi>\xi_0), \tag{A.25}$$

which has to be solved under the condition $H_0(\xi_0)=1$.

Substitution of representation (A.24) in the dynamic boundary condition (A.23) leads to the differential equation for the function $B(\xi)$

$$2s_{0\xi}B_\xi + 2\sigma_0 B = -2H_0^2 - 2\sigma_0 H_0 H_{0\xi} s_{0\xi} + 2H_0 H_{0\xi}(1-\sigma_0)\xi, \quad (z=1), \tag{A.26}$$

where dynamic boundary condition for the leading term (A.14) and Equation (A.25) have been used to simplify the right-hand side. Let $B(\xi) = b(\xi) - \sigma_0 H_0^2(\xi)/2$, then Equation (A.26) becomes

$$s_{0\xi}b_\xi + \sigma_0 b = -H_0^2\left(1 - \frac{1}{2}\sigma_0^2\right) + H_0 H_{0\xi}(1-\sigma_0)\xi. \tag{A.27}$$

The latter equation is used to compute $b(\xi)$ and $B(\xi)$ thereafter. The initial value $b(\xi_0)$ is recovered using condition (A.8), which gives $s_1(\xi_0, 1) = 0$. Taking into account that

$$s_1(\xi_0, 1) = -1 - \frac{\sigma_0}{2} - \frac{1}{2}s_{0\xi\xi} + b(\xi)$$

and

$$s_{0\xi\xi} = -\sigma_0 + \frac{1-\sigma_0}{v(\xi)}, \tag{A.28}$$

we obtain

$$b(\xi_0) = 1 + \frac{1-\sigma_0}{2v(\xi_0)}. \tag{A.29}$$

The above problem is solved numerically through a space-marching procedure which is started at a position $\xi = \xi_0$ where the angle between the free surface and the body contour is equal to a threshold value. At that point the local thickness of the jet $h(\xi_0)$ and the local value of the modified velocity potential $S_0 = S(\xi_0, h(\xi_0))$, as provided by the numerical solution in the remaining fluid domain, are used as starting values for the shallow-water solution. The step $\Delta\xi$ used to advance the system of shallow-water equations is set to be one half of the first panel on FS closest to the shallow-water boundary SW.

From the definitions, at $\xi = \xi_0$ we have $H(\xi_0) = 1$ and $s_0(\xi_0) = S_0$ with $\varepsilon = h(\xi_0)$ and $S_0 = S(\xi_0, \varepsilon)$. Then, from Equations (A.19) and (A.20), $v(\xi_0)$ and $s_{0\xi}(\xi_0)$ are computed, respectively. Through iterative solution of Equation (A.18) the constant D is derived and the initial value $b(\xi_0)$ is provided by Equation (A.29). By using Equations (A.25) and (A.28) an estimate of the free-surface slope at $\xi = \xi_0$ can be also obtained as

$$H_{0\xi} = \frac{H_0}{s_{0\xi}}\left(-2 + \sigma_0 - \frac{1-\sigma_0}{v}\right). \tag{A.30}$$

Starting from these values, the solution is advanced with a step $\Delta\xi$. Equation (A.18) is first solved iteratively to get the function v at the new location $\xi_0 + \Delta\xi$. Then, Equations (A.20) and (A.19) are used to compute $s_{0\xi}$ and s_0 at $(\xi_0 + \Delta\xi)$, respectively, while the jet thickness H_0 is directly given by the discretized form of Equation (A.25). Equation (A.30) then gives $H_{0\xi}(\xi_0 + \Delta\xi)$ which is used in Equation (A.27) to get $b(\xi_0 + \Delta\xi)$ and then the second-order correction of the potential $s_1(\xi_0 + \Delta\xi, z)$ through Equation (A.24). This space-marching procedure is carried out until a very small thickness is reached. Once the above procedure has been completed, the local shape of the free surface and the corresponding distributions of both the velocity potential and its normal derivative along the free surface and on the wetted part of the body are available.

References

1. A.A. Korobkin and D.H. Peregrine, The energy distribution resulting from an impact on a floating body. *J. Fluid Mech.* 417 (2000) 157–181.
2. T. Vinje and P. Brevig, Nonlinear ship motion. In: J.C. Dern and H.J. Haussling (eds.), *Proceedings of the 3rd International Conf. Num. Ship Hydrodyn.* Paris, France: (1981) pp. 257–268.
3. O.M. Faltinsen, Numerical solutions of transient nonlinear free-surface motion outside and inside moving bodies. In: J.V. Wehausen and N. Salvesen (eds.), *Proc. of the 2nd Int. Conf. on Num. Ship Hydrodyn.* Berkeley, USA: (1977) 347–357.
4. T. Vinje, On small-time expansion of nonlinear free surface problems. *J. Engng. Math.* 28 (1994) 173–190.
5. A.A. Korobkin and G.X. Wu, Impact on a floating circular cylinder. *Proc. R. Soc.* London 456 (2002) 2489–2514.
6. A.C. King and D.J. Needham, The initial development of a jet caused by fluid, body and free-surface interaction. Part 1. A uniformly accelerating plate. *J. Fluid Mech.* 268 (1994) 89–101.
7. L.I. Sedov, Floating wedge impact. *Tr. Tsentr. Aerodin. Inst.* 152 (1935) 27–31.
8. Z.N. Dobrovol'skaya, On some problems of similarity flow of fluid with a free surface. *J. Fluid Mech.* 36 (1969) 805–829.
9. J.M. Oliver, *Water Entry and Related Problems*. Oxford, UK: Ph.D. Thesis, University of Oxford (2002).
10. H. Wagner, Über Stoss- und Gleitvorgänge an der Oberfläche von Flüssigkeiten. *ZAMM* 12 (1932) 193–215.
11. L.V. Ovsyannikov, On the bubble upflow. In: *Some Problems of Mathematics and Mechanics*. Leningrad: Siberian Branch of Academy of Sciences of the USSR (1970) pp. 209–222.
12. P. Tyvand and T. Miloh, Free-surface flow due to impulsive motion of a submerged circular cylinder. *J. Fluid Mech.* 286 (1995) 67–101.
13. A.H. Nayfeh, *Perturbation Methods*. New York, USA: Wiley-Interscience (1976) 415 pp.
14. J.D. Cole and J.K. Kevorkian, *Perturbation Methods in Applied Mathematics*. Telos: Springer-Verlag (1981) 558 pp.
15. X. Mei, Y. Liu and D.K.P. Yue, On the water impact of general two-dimensional sections. *Appl. Ocean Res.* 21 (1999) 1–15.
16. A.A. Korobkin and A. Iafrati, Jetting by floating wedge impact. In: M. Landrini, E.F. Campana and A. Iafrati (eds.), *Proceeding of the 19th International Workshop on Water Waves and Floating Bodies*. Cortona, Italy: (2004) pp. 75–78.
17. Y.M. Scolan and A.A. Korobkin, Three-dimensional theory of water impact. Part 1. Inverse Wagner problem. *J. Fluid Mech.* 440 (2001) 293–326.